Computational high-resolution optical imaging of the living human retina

Nathan D. Shemonski[1,2], Fredrick A. South[1,2], Yuan-Zhi Liu[1,2], Steven G. Adie[3], P. Scott Carney[1,2], Stephen A. Boppart[1,2,4,5,*]

[1]*Beckman Institute for Advanced Science and Technology, University of Illinois at Urbana-Champaign, 405 North Mathews Avenue, Urbana, Illinois 61801, USA*
[2]*Department of Electrical and Computer Engineering, University of Illinois at Urbana-Champaign, 1406 West Green Street, Urbana, Illinois 61801, USA*
[3]*Department of Biomedical Engineering, Cornell University Cornell University, Ithaca, New York 14850*
[4]*Departments of Bioengineering, University of Illinois at Urbana-Champaign, 1304 West Springfield Avenue, Urbana, Illinois 61801, USA*
[5]*Department of Internal Medicine, University of Illinois at Urbana-Champaign, 506 South Mathews Avenue, Urbana, Illinois 61801, USA*
**boppart@illinois.edu*

I.   System diagram

The experiments performed in this article were obtained with a custom-built combined *en face* OCT and spectral-domain (SD) OCT system as specified in the Methods section. Figures S1 and S2 depict schematics of the optical setup. The optical setups resulted in approximately 700 µW incident on the cornea, adhering to the ANSI Standard[25] for a moving beam.
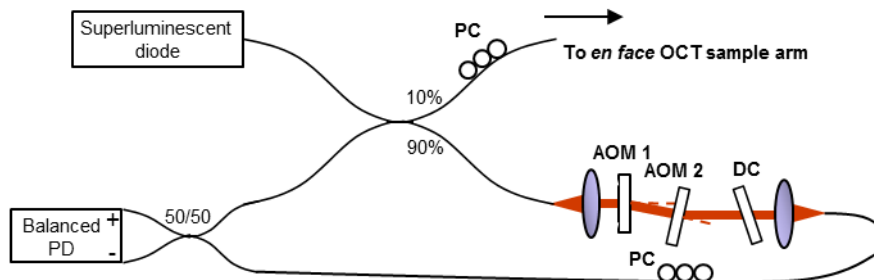

Figure S1| Schematic of *en face* OCT interferometer. PD: photodiode, PC: polarization controllers, AOM: acoustic optic modulator, DC: dispersion compensation.
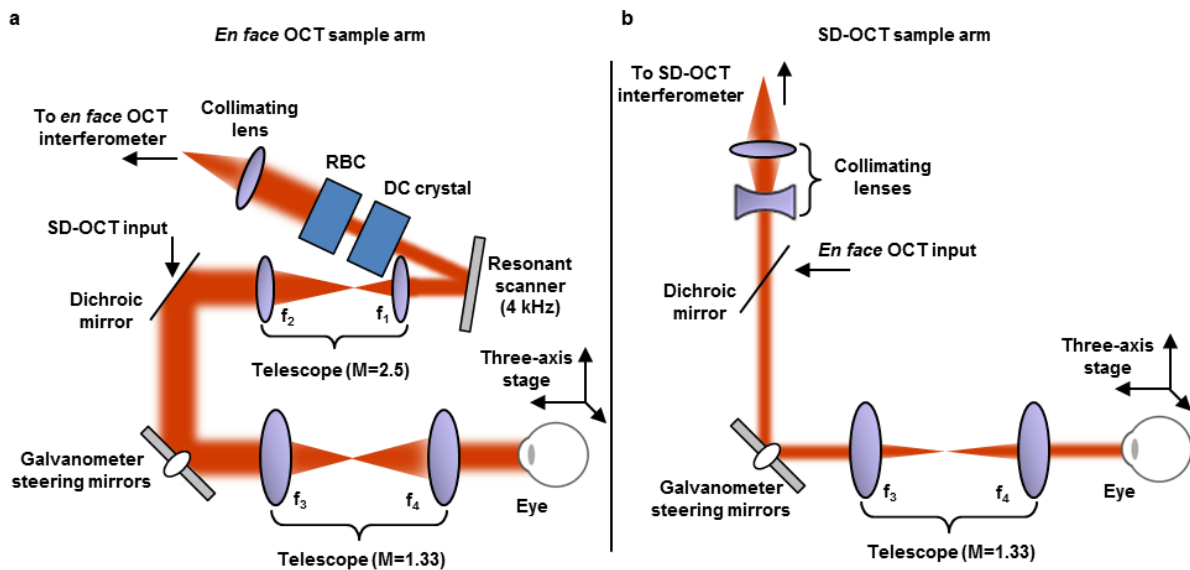

Figure S2 | Schematics of *en face* and SD-OCT sample arms. a, Schematic of en face OCT sample arm. The light enters from the fibre end labelled in Fig. S1. **b,** Schematic of SD-OCT sample arm. Both the *en face* OCT and SD-OCT beams scan the same region of the retina. RBC: reflective beam compressor, DC: dispersion compensation.

II.   Automated aberration correction

The fully-automated aberration correction algorithm was developed by combining two techniques. Initially, large, bulk aberrations were detected using a technique which computationally mimics a Shack-Hartmann wavefront sensor[16], and was computationally applied to the data based on a Fourier-optics description of the complex OCT point-spread function[15]. This consists of a forward Fourier transform, multiplication of the phase filter, and inverse Fourier transform. The correction of bulk wavefront errors was sufficient to reveal the general structure of the cone photoreceptors. A peak detection metric was then used in conjunction with a guide-star based algorithm[17] which iteratively detected and fine-tuned the aberration correction. Before these two steps were applied, the spatial 2-D Fourier content of the OCT signal was centred (i.e. demodulated) by averaging the power spectrum along each axis, fitting with a Gaussian function, and measuring the centre of the power spectrum. The spectrum was then centred in the Fourier domain. The full algorithm required 1.2 seconds per frame in MATLAB on an Intel® Xeon® CPU E-5-2667 v2 @ 3.30 GHz.

Figure S3 shows the improvement gained with the guide-star based fine tuning. Figure S3a and S3b show aberration correction with only the first step of the automated procedure, which only corrected for large, bulk aberrations. Figure S3c and S3d show the final image after the addition of the automated fine-tuning aberration correction. The improvement can also be seen with the improved visibility of Yellott's ring[26] which is a peak in the 2-D spatial Fourier transform corresponding to density of the regularly-packed cone photoreceptors. Figure S3e shows the power spectrum angularly averaged in polar coordinates. The radial polar axis is the horizontal axis of Figure S3e. In the non-aberration corrected OCT frame no peak can be seen. After bulk aberration correction, a peak from Yellott's ring can be seen. After the fine-tuned correction, the peak from Yellott's ring becomes further visible.

To further show the improvement of the fine-tuned correction, Figure S3f, shows vertical and horizontal traces through the zoomed images from Figure S3b and S3d. The locations of the traces are marked by the dashed white lines in Figure S3d. Due to the type of aberration corrected after the fine-tuned correction,

different improvements are observed along the vertical and horizontal traces. First, after the fine-tuned correction, improved resolution and SNR can be seen in the vertical trace (highlighted with arrows). This was due to the residual smearing due to aberrations along the vertical axis after only bulk correction. Next, the horizontal trace shows only improved SNR (highlighted with arrows) which is due to the improved constructive interference and resolution along the vertical axis. This can also be seen in Figure S3b and S3d where the resolution along the horizontal axis remains the same while resolution along the vertical axis is improved in Figure S3d. To clearly demonstrate the improvement, the traces were averaged over a length of approximately 30 µm along each orthogonal axis.
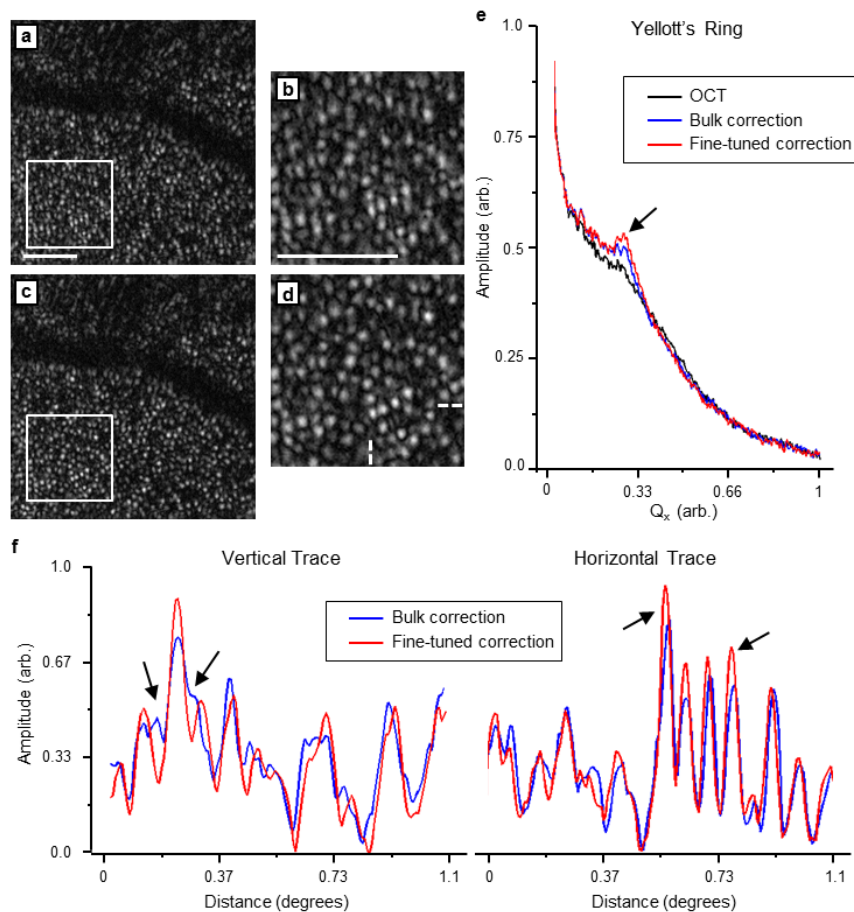

Figure S3 | Bulk and fine-tuned aberration correction. a and **b**, Computational correction of only large bulk aberrations. **c** and **d**, Fine-tuned computational correction using a guide-star. **e**, Radial average of power spectrum of original OCT frame (Fig. S4a), bulk-corrected frame (a), and fine-tuned corrected frame (c). The peak indicated by the black arrow is Yellott's ring. **f**, Vertical and horizontal traces through the zoomed images, (b) and (d). The locations of the traces are marked by the dashed white lines in (d), and were also averaged along each orthogonal axis approximately 30 µm. After the fine-tuned correction, improved resolution and SNR can be seen in the vertical trace (highlighted with arrows), while for the horizontal trace, only improved SNR is observed (highlighted with arrows). Scale bars represent 0.25 degrees.

III.   Phase stabilization

The phase of the processed *en face* OCT data was extremely susceptible to motion along the axial motion. Even small, sub-wavelength motion can create large jumps or discontinuities in the phase, and even at a frame rate of 10 FPS, motion along the optical axis from the participant's head was too large for aberration correction. In addition, the modulation induced by the AOMs was not synchronized with the scanning system, and thus itself induced phase noise if not corrected. To correct the phase of a single frame, each axis was processed separately, but in the same manner. First, the angle was unwrapped along the given axis and averaged along the orthogonal axis. The angle of the resulting line of data was then conjugated and added back to the phase of each line of the original data. This process was repeated twice along each axis. After phase stabilization, the automated aberration correction algorithm was applied. Figure S4 shows the result of applying aberration correction with and without phase correction. Figure S4a shows the original *en face* OCT frame. Figure S4b and S4c show the phase of the *en face* OCT frame before and after phase correction respectively. After phase correction, the phase shows a much more uniform pattern. Figure S4d shows the result of applying the aberration correction technique to the data with uncorrected phase. The image becomes completely scrambled. Finally, Figure S4e shows the final result of aberration correction with the phase-corrected data. Cone photoreceptors are clearly visible throughout the field-of-view.
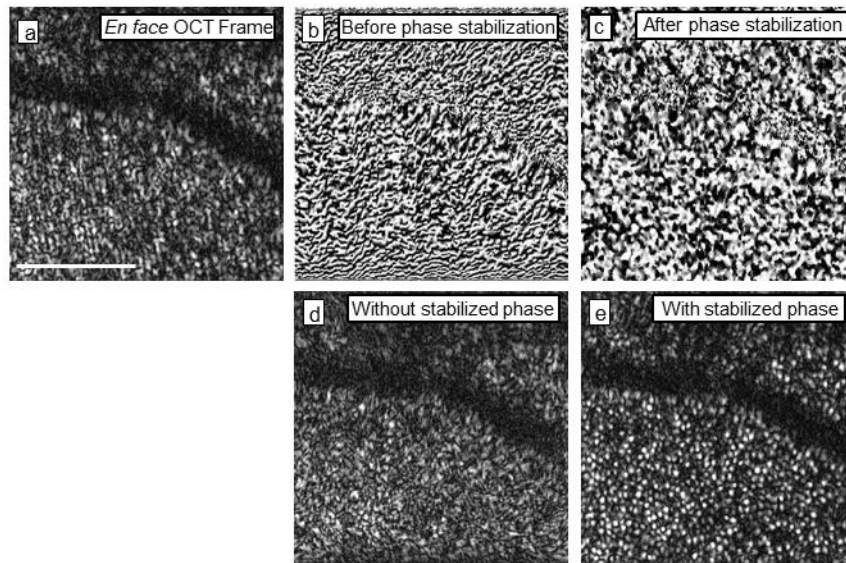
Figure S4 | Aberration correction with and without phase stabilization. a, Original, uncorrected *en face* OCT frame. **b**, Sine of the measured phase of the *en face* OCT frame before phase stabilization. **c**, Sine of the measured phase of the *en face* OCT frame after phase stabilization. **d**, Computational aberration correction without stabilized phase. **e**, Computational aberration correction with stabilized phase. Scale bar represents 0.5 degrees.

IV.   Multiple scattering

Here we describe an experiment which was designed to compare computational reconstructions with and without the influence of multiple scattering. First, a phantom consisting of point-like scatterers (titanium (IV) oxide particles, < 5 μm in a polydimethylsiloxane (PDMS)-silicone substrate) was imaged with a 1,300 nm SD-OCT system as described previously[18]. This phantom presented relatively dense scattering. Computational refocusing from this phantom is shown in the top row of Figure S5. On the left, an out-of-focus *en face* plane is shown with the corresponding computationally refocused plane in the centre. The focus was physically shifted and a second in-focus *en face* plane was extracted from the 3-D dataset. When compared to the in-focus acquisition, the refocused plane presented a lower quality image (highlighted by arrows in Figure S5.) which was attributed to a high occurrence of multiple scattering[27]. This was similar to a previous cross-validation where in-focus and re-focused data were compared[28]

A second phantom was imaged in a similar out-of-focus then in-focus manner. The second phantom consisted of two layers of PDMS without any scatterers. The interface between the two layers gave a highly-directional reflection with scattering structures resulting from imperfections in the layer. The

results can be seen in the bottom row of Figure S5. Although the out-of-focus acquisition (far left) shows no distinguishable features, the refocused (middle) and in-focus (far right) frames match almost perfectly. This is hypothesized to be due to the low levels of multiple scattering.
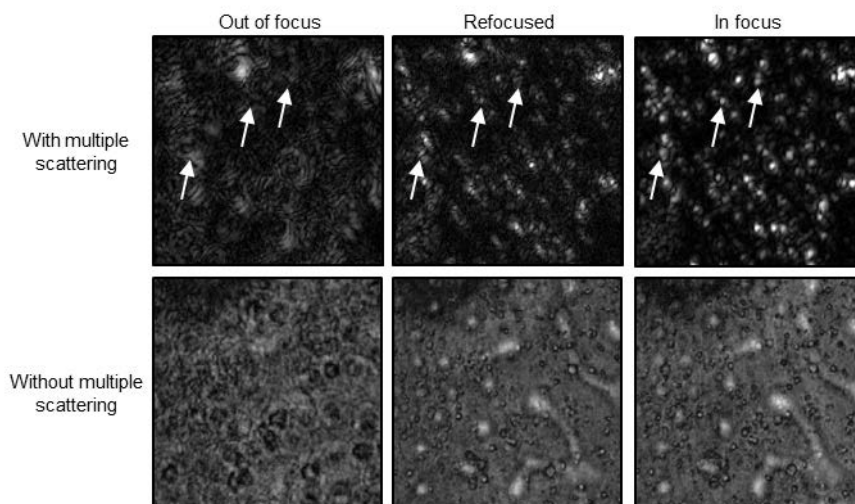

Figure S5 | Refocusing with and without multiple scattering. Top row shows point-like scatterers initially imaged out-of-focus, then refocused. The result is compared to an in-focus acquisition. Bottom row shows the same experiment with a specular-like reflection on the same instrument with the same imaging parameters. The refocused image for the specular-like reflection more closely matches the in-focus acquisition due to the low levels of multiple scattering.

When reconstructing photoreceptor cells in Fig. 1, the strength of the defocus and aberrations were similar to the experiments shown in Fig. S5, though the reconstructions were of higher quality than for the point-scattering sample in the top row of Fig. S5. We therefore hypothesize that a large fraction of the photons collected from the IS/OS junction were singly-scattered. The low level of multiple scattering was likely a result of both confocal and coherence gating as shown schematically in Fig. S6. For simplicity, only the three strongest scattering layers are drawn: the retinal nerve fibre layer (RNFL), inner-segment outer-segment (IS/OS) junction, and the retinal pigment epithelium (RPE). The blue downward arrows represent the illumination beam of light incident on the tissue. Initial back-scattering from the RNFL will be rejected due to the time gate which is centred on the IS/OS junction. Some of the photons, though, will be

forward-scattered (black dashed downward-facing arrows) which, if backscattered off the IS/OS and collected could disrupt the CAO reconstructions. Most of these photons are rejected by the confocal gate because they will not likely strike the IS/OS layer near the optical focus. This is due to the large separation between the RNFL and the IS/OS junction. Any further photons incident on the IS/OS junction which exhibit multiple scattering will then experience a longer time-of-flight and will be rejected by the time gate. Finally, since the IS/OS junction is the strongest scattering layer above the RPE, the single scattering from this layer will dominate any remaining stray photons which are collected.
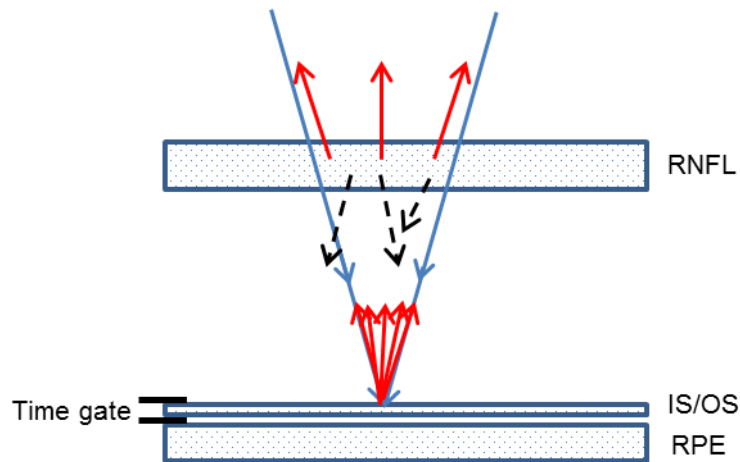

Figure S6 | Combined confocal and time gating. Out of the photons incident on the retina, only those satisfying the time-of-flight for the time gate and satisfying the position/angle scattering for the confocal gate will be collected. Due to the large separation between the RNFL and the IS/OS, these conditions strongly favour singly-scattered photons from the IS/OS junction.

V.   Imaging additional subjects

In addition to the results shown in Fig. 1, two other subjects were imaged in the perifoveal region as shown in Fig. S7 and Fig. S8. Included are SLO images showing the location of the OCT photoreceptor mosaic, the original uncorrected data, and the aberration-corrected data. Figure S7 and Figure S8 demonstrate that the techniques proposed here are repeatable over multiple subjects which would be necessary for any type of commercial or scientific adoption.
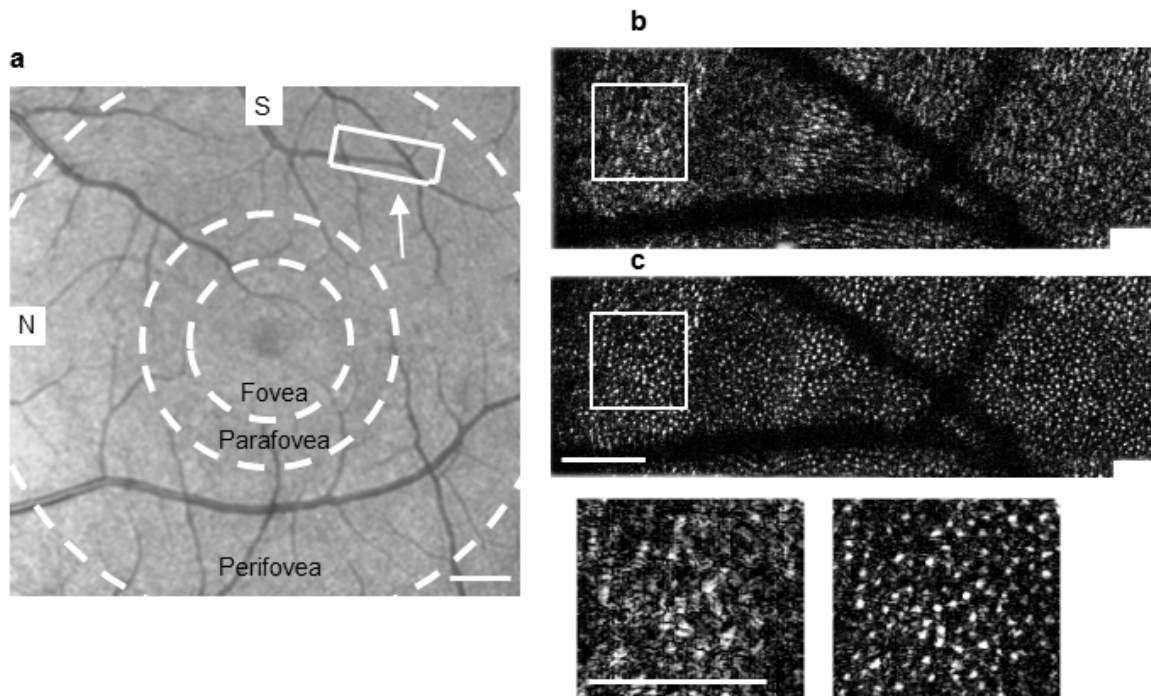
Figure S7 | Imaging Subject #2 in the perifovea. Cone photoreceptor mosaic of Subject #2 in the perifoveal region. The corrections are comparable to those seen in Fig. 1. **a**. SLO image with the location of the photoreceptor mosaic outlined. **b.** *En face* OCT mosaic before aberration correction. **c.** Photoreceptor mosaic after automated correction. Cone photoreceptors are visible throughout. Zoomed insets show further details. Scale bars represent 2 degrees in the SLO images and 0.5 degrees in the OCT images.
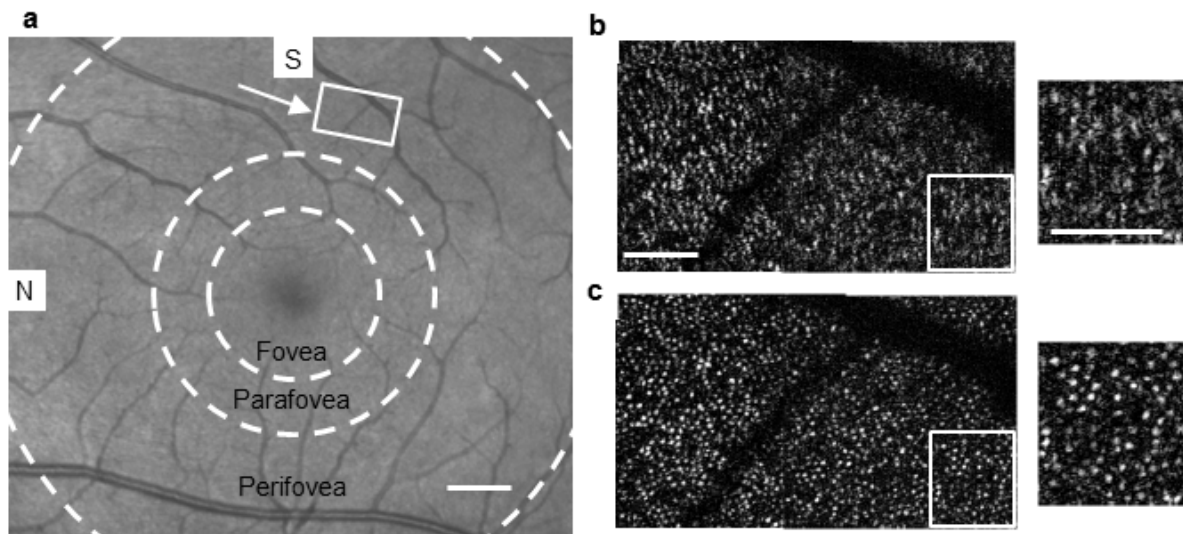

Figure S8 | Imaging Subject #3 in the perifovea. Cone photoreceptor mosaic of Subject #3 in the perifoveal region. **a**. SLO image with the location of the photoreceptor mosaic outlined. **b.** *En face* OCT mosaic before aberration correction. **c.** Photoreceptor mosaic after automated correction. Scale bars represent 2 degrees in the SLO images and 0.5 degrees in the OCT images.
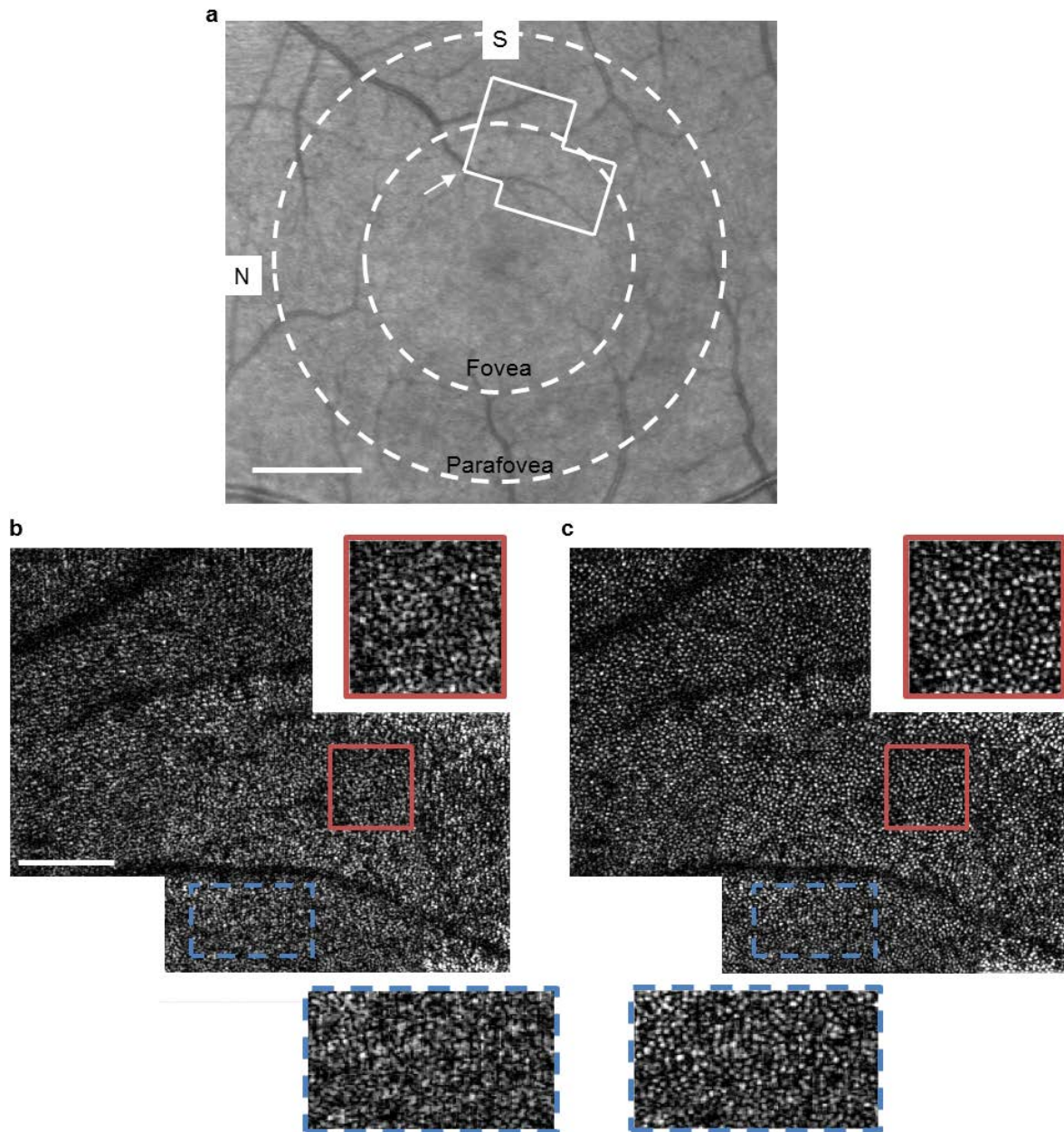
Figure S9 | Imaging Subject #2 in the fovea. Cone photoreceptors in the foveal region of the retina from Subject #2. **a**. SLO image with the location of the photoreceptor mosaic outlined. **b**. *En face* OCT mosaic before aberration correction. **c**. The same OCT mosaic after automated correction. Scale bars represent 2 degrees in the SLO images and 0.5 degrees in the OCT mosaics. The insets are zoomed by 2x.

Finally, we demonstrate imaging of the foveal cones. Fibre was. When moving closer to the fovea, the density of cones increases requiring finer resolution than when imaging the para- and perifovea cones. Figure S9 shows an image acquired from Subject #2 again, but this time in the foveal region. When compared to Fig. S7 and Fig. S8, it is clear that the density of cones has increased. The ability to resolve these foveal cone photoreceptors fully demonstrates the power of these computational approaches.

References

25   American National Standard Institute (ANSI), *American National Standard for the Safe Use of Lasers*, 2000, American National Standard Institute, Inc.

26   Yellott Jr, J. I. Spectral analysis of spatial sampling by photoreceptors: Topological disorder prevents aliasing. *Vis. Res.* **22**, 1205-1210, (1982).

27   Marks, D. L., Davis, B. J., Boppart, S. A. & Carney, P. S. Partially coherent illumination in full-field interferometric synthetic aperture microscopy. *J. Opt. Soc. Am. A* **26**, 376-386 (2009).

28   Ralston, T. S., Adie, S. G., Marks, D. L., Boppart, S. A., & Carney, P. S. Cross-validation of interferometric synthetic aperture microscopy and optical coherence tomography. *Opt. Lett.* **35**, 1683-1685 (2010).